

Multi-dimensional phenotype and long-term dynamics in individual bacteria

Lee Susman^{1,2}, Jeffrey T. Nechleba³, Hanna Salman^{3,4}, and Naama Brenner^{1,5,*}

¹Network Biology Research Center, Technion - Israel Institute of Technology, Haifa 32000, Israel

²Interdisciplinary Program of Applied Mathematics, Technion - Israel Institute of Technology, Haifa 32000, Israel

³Department of Physics and Astronomy, University of Pittsburgh, Pittsburgh, PA 15260, USA

⁴Department of Computational and Systems Biology, University of Pittsburgh, Pittsburgh, PA 15260, USA

⁵Department of Chemical Engineering, Technion - Israel Institute of Technology, Haifa 32000, Israel

*Corresponding Author: nbrenner@technion.ac.il

Abstract

Genetically identical microbial cells typically display significant variability in every measurable property. In particular, highly abundant proteins - which can determine cellular behavior - exhibit large variability in copy number among individuals. Their distribution has a universal shape common to different proteins and microorganisms; the same distribution shape is measured both in populations and in single-cell temporal traces. Moreover, different highly expressed proteins are statistically correlated with cell size and with cell-cycle time. These results indicate coupling between measurable properties in the cell and buffering of their statistics from the microscopic scale. We propose a modeling framework in which the complex intracellular processes produce a phenotype composed of many effectively interacting components. These interactions, as well as the imperfect nature of cell division events, provide a simple model that reconstructs many properties of phenotypic variability on several timescales. These include fluctuating accumulation rates along consecutive cell-cycles, with correlations among the rates of phenotype components; universal and non-universal properties of distributions; correlations between cell-cycle time and different phenotype components; and temporally structured autocorrelation functions with long (~ 10 generation) timescales.

Introduction

Phenotypic variability is a hallmark of cell populations, even when clonal and grown under uniform conditions. Variability appears in many measured cellular properties, including cell size, molecular content, organelle copy number and more. Much effort has focused in recent years on understanding this variability and its relation to stochastic processes in the cell [1, 2, 3]. When cells are viewed in a population, it is natural to treat them as independent realizations in a statistical ensemble. However it is important to remember that a clonal population is produced from a single

ancestor by growth and division. Many cellular properties are, to some degree, inherited along generations. Thus phenotypic variability is tightly connected to growth and division dynamics [4, 5, 6].

Of special interest and biological relevance is cellular protein content, which can determine functional characteristics of the cell. In microorganisms, the copy number of all proteins fluctuates considerably among clonal cells. In particular, highly expressed proteins – where number fluctuations are expected to be small – still exhibit large variability among cells. This variability displays some simple and universal features: (i) The distributions of such proteins exhibit a universal shape, shared by both bacteria and yeast cells, under a broad range of biological realizations and conditions [7, 8], and (ii) Their copy number variance scales quadratically with their mean over large datasets, including genome-wide measurements [7, 9, 10]. Such universality under a broad range of conditions suggests that the plethora of noisy molecular processes affecting protein content, are integrated to ultimately buffer cellular statistics from the molecular realm.

Recently, measurements of cellular properties such as protein content and cell size in individual bacteria over extended times have become available. These measurements provide new insight into the statistical properties of populations by revealing dynamical aspects of cell growth and protein expression [11, 12, 13, 14, 15]. Our previous work has shown that, for *E. coli*, the dynamics of protein content exhibit dynamical features on multiple timescales. On the shortest timescale, rapid fluctuations are negligible compared to the smooth exponential-like accumulation throughout the cell cycle. Over longer times, the accumulation rates vary irregularly from one cell-cycle to the next [13, 16]. Additionally, the entire trace is superimposed upon a slowly varying baseline with a typical timescale of 5-10 generations. These features are not only similar but also statistically correlated with those of cell size traces.

Importantly, the single-cell protein traces exhibit the same universal statistical properties as large populations, showing the same distribution shape and scaling between mean and variance [9, 13]. Previous analysis has shown that correlations - both along generations [17, 18] and between different properties at the same generation [13] - are crucial for reproducing the universal statistical properties. Based on the timescale separation between dynamics inside a cell-cycle and across consecutive cycles, and taking into account these correlations, a mapping model was developed for fluctuations of a single protein along generations [18]. Treating the accumulation exponents as random variables, the data were found consistent with a restraining force which keeps the process from diverging. The universal protein distribution shape was successfully reproduced from the mapping model by extracting model parameters from measured temporal traces. Nevertheless, many questions remained unanswered.

The phenomenon of universality itself, namely the collapse of distributions following rescaling,

remains an open question. Such collapse of distributions is a powerful observation that places constraints on possible underlying mechanisms [12, 14]. Within all current dynamic models, such a collapse requires a compensation between model parameters [18, 19]; why such a compensation occurs is unknown. Furthermore, the protein mapping is similar to a model recently developed for cell size [17], and suggests that protein content undergoes effective regulation through the control of cell division. However, since cell division is not known to be controlled directly by protein content the meaning of this effective regulation remains unclear. Finally, the temporal traces also revealed that the long-time (70-100 generations) average protein content and cell size are distinct among individuals, despite large fluctuations and [13]. This non-universal individual component has not been studied and is not explained by current models.

In this work we develop an approach which describes cellular phenotype as composed of multiple interrelated components. In this approach, protein content and cell size are considered the outcome of a complex, interacting multi-dimensional system inside the cell. A coarse graining is imagined, where interactions between two observables are induced by averaging over many other hidden degrees of freedom. Therefore, rather than postulating specific interactions, we focus on properties that emerge in a general class of models with effective interactions. Other essential components of the class of models considered here include: relatively short cell-cycle times, imperfect division events and at least one variable that effectively controls cell division timing. This approach provides a unified framework for statistical properties of protein and cell size and answers many of the above mentioned open questions.

We first present new experimental results that shed light on the correlations between different cellular phenotype components, specifically cell size, the content of different proteins and cell-cycle time. We also present new analysis highlighting and characterizing the individual non-universal statistics, including long-term average and correlations. These statistics complement previously studied universal statistical properties. We then present the model and its results, illustrating how it reproduces many aspects of the data over several timescales and provides an explanation for both universal and non-universal statistical properties. More generally, it demonstrates the role of multiple interacting variables in creating cellular variability and individuality.

Results

Experimental Results

Recent developments in experimental techniques allow us to follow single trapped bacterial cells for many generations and to measure various cellular properties along time [20]. In this section we present such data and analyze their dynamical and statistical properties over multiple timescales:

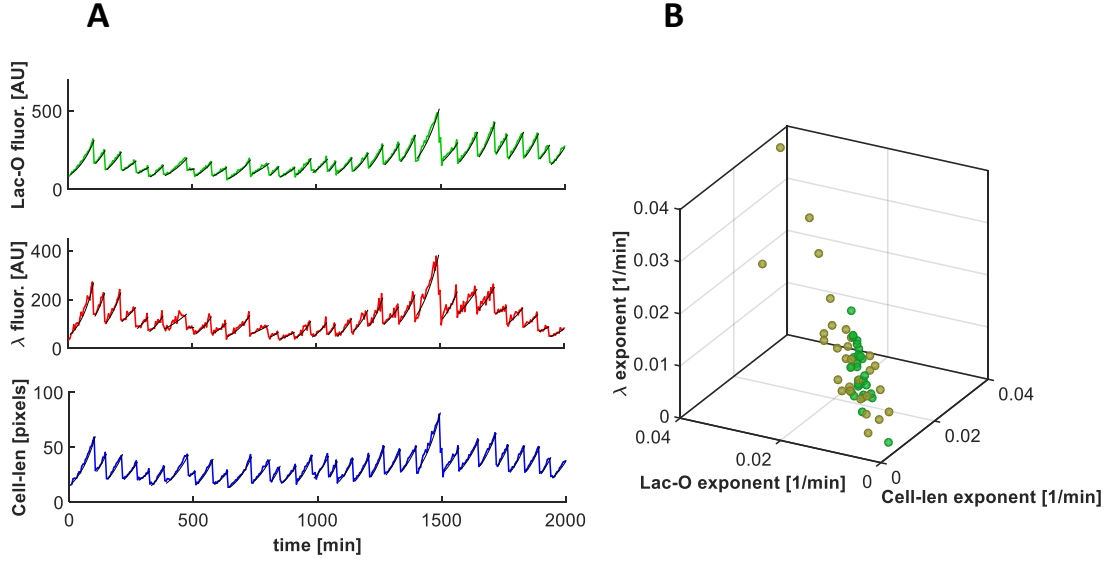


Figure 1: Correlated phenotype components in a single cell. (A) Time evolution of cellular phenotype components along multiple generations of a single trapped bacterial cell. Top: LAC promoter reporter; middle: λ promoter reporter; bottom: cell length. Cells are grown in a quasi-1D trap with their width constant, thus cell length is a good indicator of total cell size. (B) Effective exponential accumulation rates for all three components are obtained by fitting to the data (black line in A). Each dot has coordinates corresponding to the three rates. Data are pooled from two experiments (different colors, total of 61 cell-cycles). Rates span a broad range of values, with coefficient of variation 0.41 for cell-length, 0.54 for Lac and 0.5 for λ . Across this range, rates exhibit strong cross-correlations, with Pearson correlations coefficients 0.88 for length-LAC, 0.92 for length- λ and 0.9 for LAC- λ .

first, within single cell-cycles; then, across divisions over several cycles; and finally, over long times of many ($\approx 10 - 20$) generations. Parts of the data were previously published in [13] and are presented here for completeness.

Our previous work has shown that accumulation rates of cell-size and protein content are strongly correlated across generations, even for metabolically irrelevant proteins [13]. This result suggests that similar correlations may exist also between any two proteins regardless of their specific function. To test this prediction directly, we constructed bacterial strains that express two colors of fluorescent protein from two different promoters, and measured both proteins and cell size simultaneously in each cell. An example of such a three-component trace, measuring a single bacterial cell over multiple generations, is displayed in Fig. 1A. The top panel (green) displays protein expressed from a LAC operon promoter which is a metabolically important promoter in the medium used in this experiment. The middle panel (red) displays protein expressed from the λ promoter, an alien promoter derived from bacterial phage, which does not play any metabolic role in the cell. The bottom panel (blue) shows the dynamics of cell size [12, 21, 22, 23, 24]. All measured cellular properties in Fig. 1A exhibit smooth accumulation throughout the cell cycle. For cell size, it is common to describe these curves by single exponentials, consistent with experimental

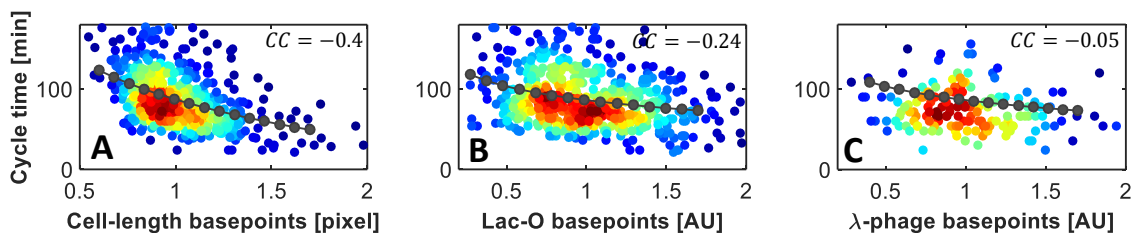


Figure 2: Cell cycle time is correlated with different phenotype components. Cycle duration as a function of cell length basepoint (A), Lac operon fluorescence basepoint (B) and λ -phage fluorescence basepoint (C), pooled from different traces. Color code represents density of the data points, and the Pearson correlation coefficients (CC) calculated for each panel is displayed. Bold black data points represent the best linear fit in log-space phenotypic coordinates. These values show a decreasing correlation strength for different components: cell size is highest, then a metabolically relevant protein, finally an alien irrelevant protein. Panels A,B show a total of 540 cell-cycles from 12 different traces; panel C shows a total of 155 cell-cycles from 4 different traces.

measurements showing that the growth rate is proportional to the instantaneous size [25]. Using the exponential fit for all components (black lines), a set of three accumulation rates can be defined for each cycle. These are presented as dots in a three-dimensional scatter-plot, one point for each cycle, in Fig. 1B. The figure shows that the three accumulation rates span a broad range of values, consistent with previously published results on cell size [13, 16]. Across this range, these rates are strongly correlated on a cycle-by-cycle basis. Such high cross-correlations support the idea that the smooth accumulations of all measured properties reflect a multi-component dynamical system, coherent throughout the cell cycle. In the spirit of this idea we term the measured cellular properties components of the multi-dimensional phenotype (or phenotype components).

In contrast to the smooth accumulation of phenotype components during cell growth, cell division defines a significant discrete event that disrupts their dynamics. These division events simultaneously distribute all phenotype components between newborn cells. Thus, despite the disruption and possible decoherence induced by division, the common cycle time may provide an additional coupling mechanism between the different phenotype components. Fig. 2 shows how cell-cycle duration is correlated with initial cell-length (A) as well as with initial protein content (B,C) in the same individual cell. The correlation is strongest for cell-length, weaker for a metabolically relevant protein, and finally very weak for a non-relevant protein marker. The negative correlation of cell-cycle time with measures of cell size is in line with previous results [17, 26, 21, 27, 23, 22]. On the other hand, its correlation with protein content is less understood and may be an indirect result of coupled dynamics between phenotype components. This possibility will be further discussed in the context of the model below.

On the longest available timescale of the entire trace, one may compute statistics over time and compare them between individual traces. As opposed to the above described correlations, which can be extracted from any large collection of separate cell cycles, here long enough traces are re-

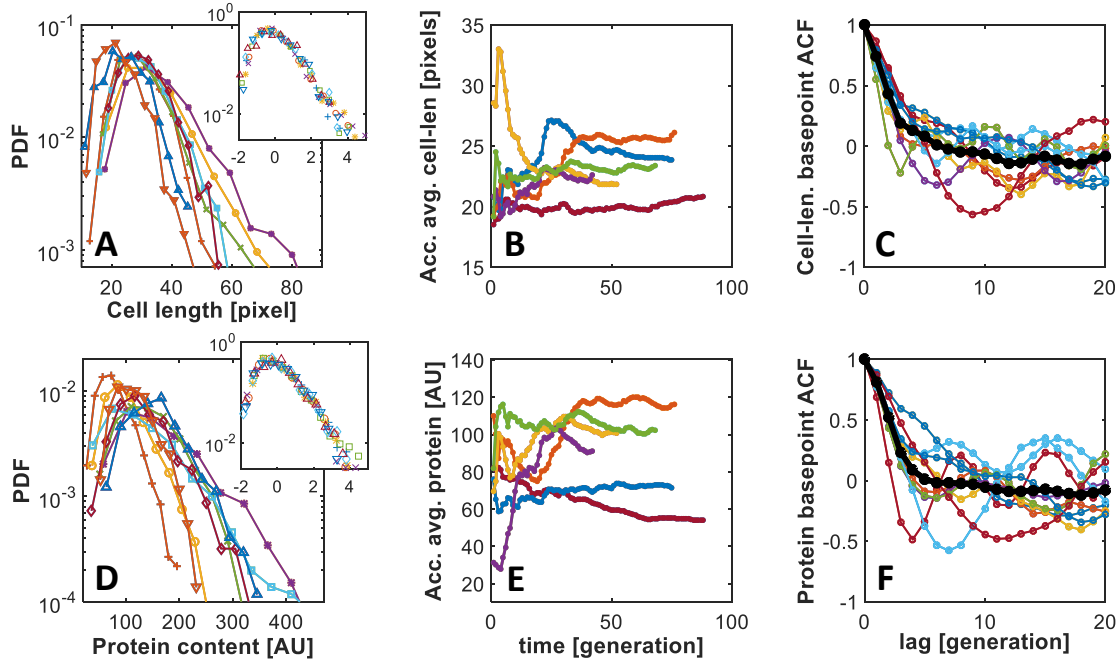


Figure 3: Long-term individual trace statistics. Distributions of cell-length (A) and protein fluorescence (D) in physical units, calculated along eight different traces (color code). Insets: the same distributions in scaled variables. Both phenotype component exhibit a collapse of scaled distributions onto a single universal curve. Accumulating mean cell-length (B) and protein fluorescence (E) along the traces, as a function of time window of averaging. Despite large fluctuations in each trace, long-term averages converge to distinct individual values at long times. Autocorrelation of basepoint values for individual traces (colored lines), both for cell-length (C) and for LAC regulated protein (F). Average over all traces is displayed by a black line. The discrete time series of effective exponential accumulation rates also exhibit similar features (see SI5).

quired which allow large temporal sampling for each individual cell. Fig. 3 shows the distributions along time of cell-size (A) and protein content (B), with the distinct scale manifested by their different centers and widths. The universal shape after scaling is shown in the respective insets (see [13]). Another way to observe the distinct scale of each trace is by averaging over an increasing time window. The results of such averaging are presented for cell-size (C) and protein content (D) as a function of window size; the entire trace average is the last point in each curve. Both these presentations of the same data show that, although all traces fluctuate considerably, each one converges to a distinct average value over the entire length of time. Temporal averages span a range of up to two-fold for protein content and up to 20% for cell size. Analysis of single-cell traces measured in another lab [11] reveal a similar individuality in temporal averages (see SI1).

The second statistical property which is computed separately along time for each trace is the autocorrelation function. To disentangle the long-term dynamics from the short accumulation and division cycles, we consider the phenotype components at the beginning of consecutive cell cycles (basepoints), forming a discrete time-series. Their autocorrelation functions reveal a temporal structure spanning many generations, as seen in Fig. 3C,F. For some of the traces, damped oscillations are clearly seen. The typical periods and amplitudes of these oscillations are distinct for each individual trace (see also [28]). As a consequence of this incoherency, these structures are washed by averaging traces (black lines in in Fig. 3C,F).

Next we discuss a new theoretical modeling framework that accounts for the above presented results.

Effective Interactions Model

Our guiding hypothesis in constructing the model is that the cell constitutes a complex system composed of many interacting variables. When we measure any specific cellular property, such as protein content, we are probing the result of this complex system. When we measure several properties simultaneously, an effective interaction between them will be observed. This should not be interpreted as a simplistic causal relation, but rather as an effective description of their participation in the large dynamical system that is the cell, and which may contain many other hidden variables.

We consider N observable phenotype components represented by a vector of time-dependent quantities $x^{(1)}, x^{(2)}, \dots, x^{(N)}$. Specific examples for which measurements are presented are copy number of proteins and cell size. As seen in the data, these components accumulate approximately exponentially over the cell-cycle. Since we seek an effective description of the interactions between variables, we look for the simplest and most general interactions that are consistent with this experimental observation. Previous work has suggested that generally autocatalytic-like dynamics can

arise indirectly from linear interactions [29, 30]. In light of the above argument, we use this simple model for describing the effective dynamics within a cell cycle,

$$\frac{d}{dt}\vec{x}(t) = K\vec{x}(t), \quad (1)$$

where

$$\vec{x}(t) := \left(x^{(1)}(t) \quad x^{(2)}(t) \quad \dots \quad x^{(N)}(t) \right)^\top, \quad 0 < t < T,$$

with t denoting the time within the cell-cycle between consecutive divisions, and T the cycle duration. These dynamics are deterministic, thus rapid intra-generation fluctuations are neglected in this model, in line with the data. The entries k_{ij} of the matrix $K \in \mathbb{R}^{N \times N}$ represent the rates by which $x^{(i)}$ is affected by $x^{(j)}$. We assume the existence of a positive eigenvalue of this matrix, but otherwise its exact details are arbitrary. We will be primarily interested in properties of the resulting dynamics which are insensitive to these exact details (see SI2).

Moving up the time-scale hierarchy to the inter-generation dynamics, our model must account for cell divisions. Three effects are taken into account concerning division: first, the distribution of phenotype component between daughter cells; second, the determination of division time; and finally, the inheritance properties of the effective interaction matrix K .

To address the abrupt distribution of phenotype components between daughter cells, we denote the phenotype vector in the n th cell cycle by $\vec{x}_n(t)$, and its baseline value at the beginning of the cycle $x_n^{(j)} := x_n^{(j)}(0)$. The division event distributes fractions $f_n^{(j)}$ (generally different for each component) and $1-f_n^{(j)}$ to each daughter cell, and thus connects the phenotype component at the current cycle-end with its value at the beginning of the next cycle. Experimental evidence shows that for bacteria these division fractions are Normally and narrowly distributed around $\frac{1}{2}$ with a typical standard deviation $\sigma \approx 0.1$ [13]. We therefore take the per-component division ratios $f_n^{(j)} \sim \mathcal{N}\left(\frac{1}{2}, \sigma^2\right)$, linking consecutive generations such that for each $1 \leq j \leq N$

$$x_{n+1}^{(j)} = f_n^{(j)} \cdot x_n^{(j)}(T_n),$$

with T_n the duration of the n th cell-cycle, which needs to be specified next. Experiments show that this duration is correlated with the value of measured phenotype components at the start of the cell-cycle, as observed in Fig. 2. Therefore we allow all phenotype components to play a role, to various degrees, in determining cell-cycle time:

$$T_n = \bar{T} - \sum_{i=1}^N \beta_i \ln x_n^{(i)} + \xi_n, \quad (2)$$

where $\beta_i \geq 0$ are parameters describing the contribution of each phenotype component to the

global regulation of cell-cycle time. The special case of a single nonzero β will also be considered. \bar{T} is a typical scale, independent of the regulation, and ξ_n is a random variable with average $\langle \xi \rangle = 0$ [18]. We note that a process with exponential accumulations and divisions is unstable to fluctuations and generally diverges for long times (as discussed previously in the context of protein dynamics [18] as well as cell size dynamics [17]). Therefore, in addition to being consistent with the data, some form of negative correlation between T_n and the phenotype components is mathematically required to keep the process stationary [18].

Finally, it should be specified how the effective interaction rules, represented by the matrix K , transmit to the next generation at cell-division. We assume that basically the global metabolic cell state is inherited from one generation to the next, with only slight variation in the effective interactions that could be viewed as another outcome of the imperfect division. Therefore $K_{n+1} = K_n + \varepsilon_n$, where $\varepsilon_n \in \mathbb{R}^{N \times N}$ has a variance which is small relative to the elements of K_n (less than 1%). Alternatively, a constrained random walk on the elements of K does not alter model results. For some properties the inheritance can even be assumed perfect, i.e. K remains strictly fixed across cell division (see SI2).

Model results

Within a cell-cycle, given K , T and $\vec{x}(0)$ – the basepoint vector – the solution of Eq. 1 is a deterministic and smooth trajectory for all phenotype components:

$$\vec{x}(t) = \sum_{i=1}^N c^{(i)} e^{\lambda_i t} v_i \quad 0 < t < T. \quad (3)$$

Here $\{\lambda_i\}_{i=1}^N$ are the eigenvalues of K , $\{v_i\}_{i=1}^N$ are the respective eigenvectors, and $c := \begin{pmatrix} c^{(1)} & c^{(2)} & \dots & c^{(N)} \end{pmatrix}^\top$ are the projections of $\vec{x}(0)$ on the eigenbasis $V = [\vec{v}_1 \dots \vec{v}_N]$, i.e.

$$c = V^{-1} \vec{x}(0).$$

Where eigenspace is arranged such that λ_1 is the largest positive eigenvalue.

The resulting in-cycle trajectories are a linear combination of exponentials (Eq. 3). Nevertheless, each trajectory can be described, to a good approximation, by a single exponential function with an *effective exponential* accumulation rate. Fig. 4A illustrates a model trajectory of one phenotype component out of $N = 5$, fitted to an effective exponential function $x^{(j)}(t) = a^{(j)} e^{\alpha^{(j)} t}$ over one cell cycle, demonstrating that the solution given by Eq. 3 is well described by a single exponential accumulation curve. In general, over long time-scales, a linear combination of exponential functions would be dominated by the leading exponent λ_1 . However, biological constraints limit the

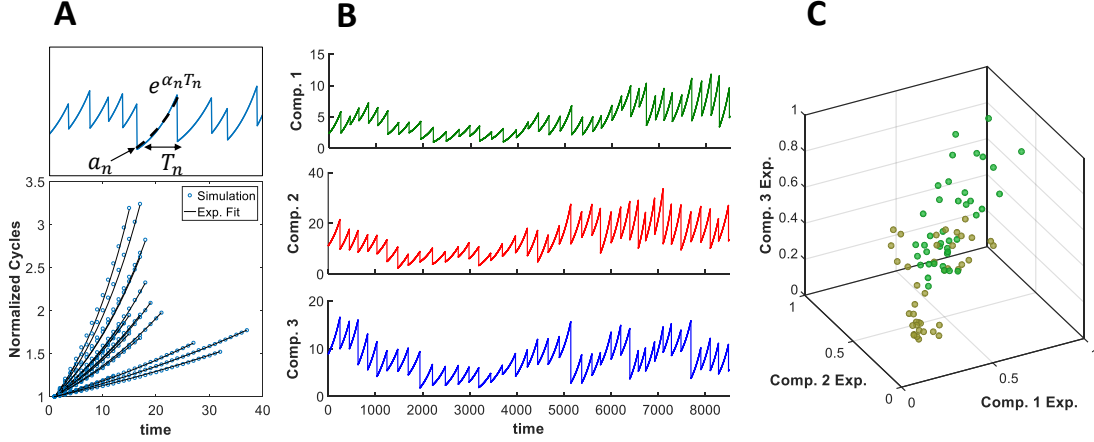


Figure 4: Multi-dimensional phenotype traces in the model. (A) Top: Example of model trace resulting from multi-dimensional interaction system and division. Due to the short cell-cycle time, in-cycle portion of the trace can be approximated by an exponential (black line), although in reality they are composed of a sum of exponentials. Bottom: Cell-cycle traces normalized to initial time and to value 1 at the cell-cycle start, emphasizing the variability between generations of the effective exponents. (B) Time evolution of three model phenotype components taken from a simulation of a 5-dimensional system. The plot shows 40 generations. (C) Effective (empirically fitted) exponential growth rates of the three shown phenotype components, from two different simulation runs (color code). Positive correlation between the exponents requires small changes in the interaction matrix K between generations, to break a sum-rule which occurs otherwise as a result of the dominance of one eigenvalue. Thus, in the model the positive correlations reflect the fact that changes in metabolism affect different phenotype components in a similar manner.

cell-cycle to relatively short times, over which the components increase by only a factor of ~ 2 . Due to this limited time the effective exponent depends on all eigenvalues as well as on the prefactor of each exponent. As a result of this dependence and of the imperfect nature of division, fluctuations emerge in the effective exponents from one generation to the next. These fluctuations are caused by the distribution of random fractions at the beginning of each cycle, which in turn reshuffles the prefactors of exponents in Eq. 3. Although the eigenvalues and eigenvectors also slightly change at division with the change of K , they have a negligible effect and similar fluctuations are seen also for a matrix K , which is fixed along generations (see SI2). Examples of the effective exponentials for one phenotype component, all normalized to 1 at the cell-cycle start, are presented in Fig. 4A (lower panel) as black fitting curves. Our previous work has shown that variability in the exponential accumulation rates among generations is significant ($CV \approx 0.5$), and is required for obtaining the broad universal distribution of proteins from single traces [13]. This variability arises here naturally as a result of effective interactions and small noise in imperfect division, without the need to explicitly introduce a large stochastic element into the rate [18].

In Fig. 4B we show example traces of phenotype components along time produced by integrating all the model features described above. The results presented in this figure are insensitive to many properties of the matrix K , including its dimensionality and exact values (see SI2). They are also insensitive to the choice of global regulation parameters β_i ; the example presented in the

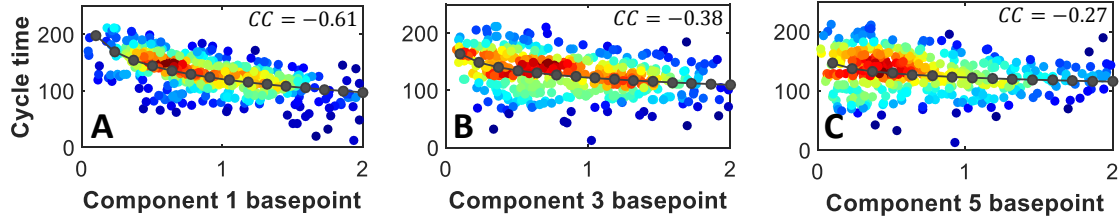


Figure 5: Empirical correlations between cycle times and phenotype components. Dependence of cycle-time on three phenotype components in our model; bold black data points represent the best linear fit in log-space phenotypic coordinates. In this simulation the cycle-time actually depends only on the first phenotype (only $\beta_1 > 0$ in Eq. 2). Global correlations of various degrees emerge between cycle times T_n and other phenotype components through their mutual interactions.

figure corresponds to the special case of only a single nonzero β . The fluctuations of the effective exponents from one generation to the next are clearly seen in all component traces. In agreement with the experimental data shown in Fig. 1, the effective exponents span a broad range of values and exhibit strong correlations (Fig. 4C).

Correlation between cell-cycle durations and phenotype components at the cycle start are presented in Fig. 5. The points in the scatter-plot are collected from many traces produced by the model with the same set of parameters, one point for each cell-cycle, analogous to the analysis of experimental data presented in Fig. 2. As expected, phenotype component 1 exhibits a strong correlation with cell-cycle time; it is the only component with a nonzero regulation parameter β . More surprisingly, effective correlations emerge between cycle duration and all other phenotype components, as seen in Fig. 5B,C (see SI3 for calculation). These indirect correlations are a result of interactions within the cell cycle and the common division times. While component 1 is special in this realization of the model, the difference between component 2 and 3 is only in the effective interactions determined by the random choice of K . Qualitatively similar results to Fig. 5 are obtained if more than one phenotype component controls division, namely more than one of the β s is nonzero. The significance of these observations to the interpretation of the experimental data will be further discussed below.

Statistical Properties

To gain a quantitative understanding of the model and resulting statistical properties, we focus on one of the phenotype components and develop a mean-field approximation for its mapping along generations. Using the effective exponent and initial baseline values, we construct the mapping as follows:

$$x_{n+1} = f_n x_n e^{\alpha_n T_n}, \quad (4)$$

where subscript j for the component of interest has been dropped. Changing to logarithmic coordinates $y_n = \ln(x_n)$, introducing a mean-field variable E_n for all contributions from other components (see SI4) and defining the additive term $\eta_n = \ln f_n + \alpha_n \xi_n + \alpha_n E_n$, we reformulate Eq. 18 as

$$y_{n+1} = (1 - \alpha\beta) y_n + \eta_n. \quad (5)$$

Here α is the effective exponent averaged over time, and $\alpha\beta$ now represents the average strength of the effective restraining force on our chosen component (see SI3). The resulting mapping is formally equivalent to a Langevin equation in discrete time [17, 18, 24]. Assuming a Gaussian distribution for η , the solution is also Gaussian with mean

$$\mathcal{M} = \frac{\langle \eta \rangle}{\alpha\beta} = \frac{1}{\beta} \left(\frac{\langle \ln f \rangle}{\alpha} + \bar{T} + \langle E \rangle \right) \quad (6)$$

and variance

$$\mathcal{S}^2 = \frac{\langle \eta^2 \rangle - \langle \eta \rangle^2}{2\alpha\beta - (\alpha\beta)^2}. \quad (7)$$

The original coordinate x_n therefore converges to a log-normally distributed random variable x with parameters \mathcal{M} and \mathcal{S} :

$$P(x) = \frac{1}{x\mathcal{S}\sqrt{2\pi}} \exp \left[-\frac{(\ln x - \mathcal{M})^2}{2\mathcal{S}^2} \right].$$

We note that \mathcal{S} is a "shape parameter" of this log-normal distribution: a family of log-normal distribution can be linearly rescaled to collapse to the same curve if they have the same value of \mathcal{S} . This result is similar to distributions derived previously for one-dimensional models of exponential accumulation and division [17, 18]. However, here the parameters of the distribution depend on combinations of dynamical variables along the trace. In particular there is no independent model parameter determining the average along the trace; this average emerges as a function of dynamics. The plurality of effective interactions encoded in the matrix K are reduced here to the single quantity α . The cell-cycle time regulation parameter is encoded in β . Together, these two parameters determine the restraining force $\nu = \alpha\beta$ in the effective Langevin equation, which in turn determines the distribution parameters.

Despite the additional effective mean-field variable η_n , these expressions suggest how distinct average values over traces may emerge. If each trace has a different time regulation parameter β , they would have distinct long-term averages. Moreover by Eq. 6 this average should be inversely correlated with the regulation parameter. This correlation is illustrated for model traces in SI6, and can be tested directly for the experimental phenotype traces. For each trace we compute two independent estimates: the average log-phenotype along the trace, corresponding to the model

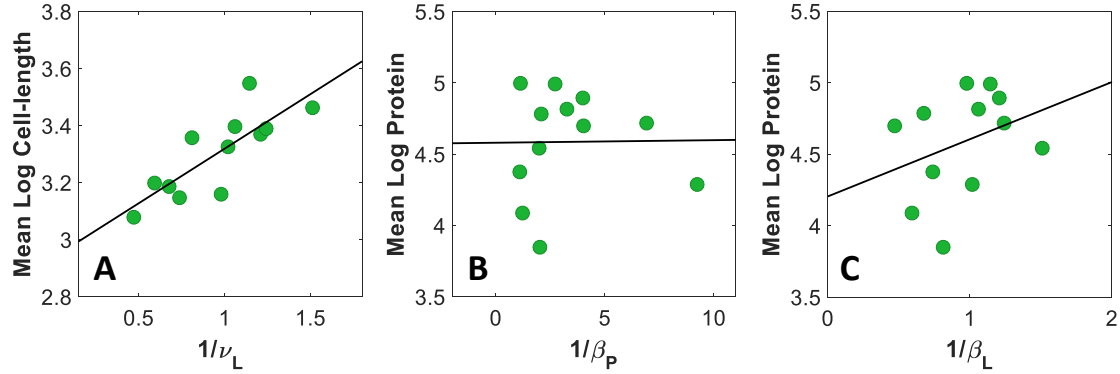


Figure 6: Non-universal trace average in experiential traces. (A) Dependence of average (log) cell length along individual traces on the measured inverse strength of restraining force on cell length, $1/\beta_L$. As predicted by Eq. 6, a linear relation is observed (correlation coefficient $CC \approx 0.8$). (B) Dependence of average (log) protein content on measured inverse strength of protein restraining force β_P . No significant dependence is seen (correlation coefficient $CC \approx 0.01$). (C) Dependence of average (log) protein content on inverse strength of cell-length restraining force $1/\beta_L$ (correlation coefficient $CC \approx 0.3$). In all panels black line represents the best linear fit to the data points. Each point corresponds to a different trace; 12 traces with a total of 540 cell-cycles.

parameter \mathcal{M} ; and the value of the time-regulation parameter β from scatter-plots (see Materials and Methods for details). The two estimates are plotted in Fig. 6A for a collection of cell-length traces, average log cell-length as a function of $1/\beta_L$, showing that the relation is linear as predicted by Eq. 6.

Fig. 6B shows the same data for a set of LAC protein traces. This protein is metabolically relevant and accordingly has a nonzero value β_P for all individual cells, as estimated from scatter-plots. In contrast to cell-length, it is seen that these two parameters of individual traces do not correlate across the collection of traces. This would imply a contradiction to the model result of Eq. 6. However, these observations can be reconciled if one assumes that cell-size directly regulates cell cycle time, whereas protein is only indirectly correlated with it (see Fig. 5 above). Under this assumption, the individual average protein should be correlated with the time-regulation parameter β_L , corresponding to cell length. This is supported by Fig. 6C (see also SI6 for model calculations). We conclude that the distinct time averages of phenotype components can be linked to measurable differences in dynamical parameters of each individual trace, when considering multiple components in parallel.

From Eq. 7 it follows that the shape parameter of the log-normal distribution depends on the strength of restraining force $\nu = \alpha\beta$, which also varies between individual traces. Why, then, is the distribution shape similar among different traces, whereas the average varies? Fig. 7 presents a possible explanation for this phenomenon. It shows the value of the shape parameter estimated directly from different traces, as a function of the estimated ν of these traces. In contrast to the log-average, here it is seen that the shape parameter S depends rather weakly on ν in the region

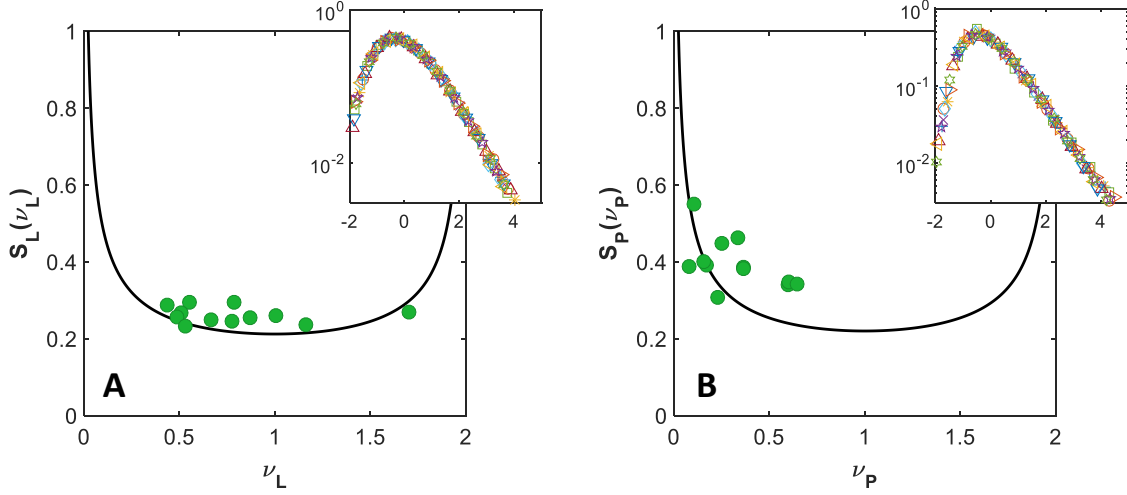


Figure 7: Universal distribution shape. Green circles depict the value of the shape parameter of the log-normal distribution for each individual trace, cell-length (A) and protein content (B). These are plotted as a function of the respective effective regulation parameters $\nu = \alpha\beta$. Black line is the theoretical prediction. For both phenotype components the shape parameter spans a relatively narrow dynamic range. Insets: Distribution of random variables drawn from scaled log-normal distributions with shape parameters corresponding to the data points.

of interest. In particular, the values measured for our traces fall within the plateau created by the function in Eq. 7. This is particularly true for cell size measurements, shown in Fig. 7A. Protein content values of the shape parameter span a slightly larger range of values. However, plotting log-normal distributions corresponding to the measured shape parameters in scaled units shows consistency with a data collapse to high accuracy (insets), for protein as well as for cell size. Thus, the range $S \in (0.3, 0.55)$ which is observed for protein content, still defines log-normal distributions with similar shapes (see SI7). These two levels of invariance, the plateau of the shape parameter and the insensitivity of the log-normal to this parameter in its measured range, are consistent with the observed universality of scaled distributions.

The second statistical property which is distinct among individual traces is the time-averaged correlation function (Fig. 3C,F) (see also [28]). Some traces exhibit damped oscillations, with varying amplitudes and frequencies, whereas others exhibit a smooth decay. First, we observe that our model traces display similar features; see Fig. 8A. Theoretically the correlation function can only be computed as an average over the ensemble of realizations. Indeed, for the mapping of Eq. 5 the result is $R_n = \frac{\langle (y_n - \mathcal{M})(y_0 - \mathcal{M}) \rangle}{S^2} \approx (1 - \nu)^n$, i.e. an exponential decay as a function of the number of generations. An analytic calculation of these correlations along time, as opposed to across the ensemble, is lacking. As a first step toward understanding these correlations, we utilize a recently established theoretical framework linking the strength of the restraining force to

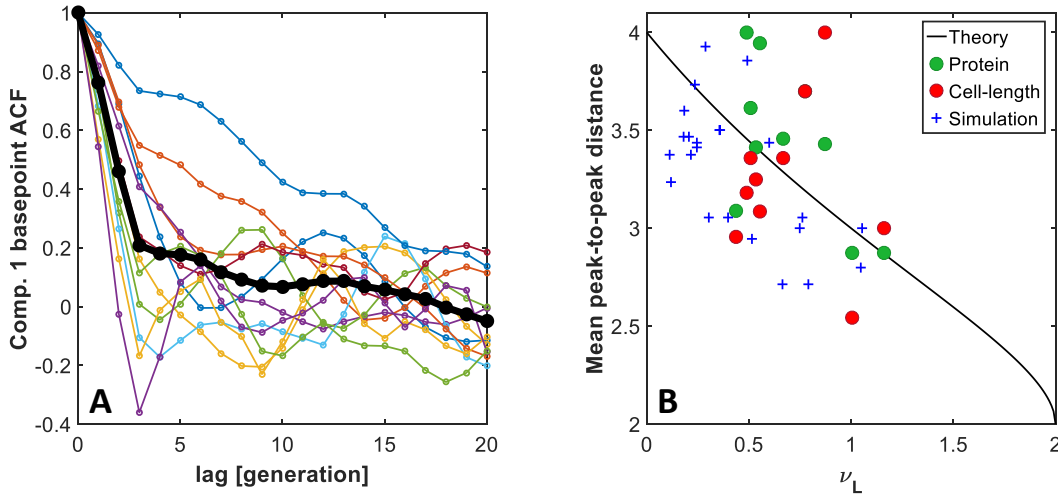


Figure 8: Temporal structure in autocorrelation functions. (A) Autocorrelation functions of model traces, showing features similar to the data: some traces oscillate with various frequencies and amplitudes. (B) Mean peak-to-peak distance as a function of restraining force parameter ν , for protein fluorescence (green) and cell length (red). Each point corresponds to an individual trace of experimental measurements. Black line represents the theoretical prediction for Gaussian noise in a discrete Langevin equation [31]. Blue crosses correspond to simulated model traces, with number of generations similar to that of the experiments. This provides an estimate of the expected spread. See SI7 for an analysis of the dependence on sample size.

the temporal structure emerging in a discrete Langevin equation [31]. In that work, the probability of oscillatory patterns being generated at random across time was estimated. Approximating the frequency of oscillations by the distance between local peaks, this distance was computed as a function of the restraining force. Fig. 8B shows this theoretical prediction (black solid line) together with the corresponding quantities computed from our experimental traces for cell size (red data points) and protein content (green data points). For comparison, the results of oscillation period from model traces are shown (blue crosses). The experimental results are not in quantitative agreement with the theory, however they are in the same level of agreement as model simulations of the same trace length. The theory becomes a better predictor of model simulations for longer traces (see SI8). Therefore the comparison in Fig. 8B shows that the data are consistent with a simple interpretation: the long-term properties of the autocorrelation function arise from purely stochastic effects, in combination with the inherent discreteness of the dynamics induced by cell-division.

Discussion

The biological cell is a complex system with a myriad of interacting processes that influence its phenotype. Nevertheless, cellular measurable properties, known to be variable among individual cells, have been mostly viewed as independent of one another. Separate studies have been carried out on cell size, protein content, metabolic state, growth rate etc. In the current work we developed an approach to cellular phenotype which explicitly focuses on its multi-dimensional nature. This

approach is rooted in dynamic measurements of several phenotype components simultaneously in individual cells, including cell size and different highly expressed proteins. Quantitative data on correlations between phenotype components over multiple timescales provide the basis for the modeling framework.

Within a cell-cycle, the model describes each phenotype component as a result of linear effective interactions with each other and with other unknown components. Our description is similar to previous work on the Hinshelwood cycle, producing effective auto-catalytic dynamics [29, 30]. However, here we take into account explicitly the finite duration of cell-cycle and the imperfect nature of division which reshuffles the different phenotype components. As a consequence, rather than a simple exponential dynamics which reflects only one timescale - the leading eigenvalue of the interaction matrix - several eigenvalues continue to contribute. This results in effective (rather than exact) exponents which vary over time and between components.

Although our model describes accumulation as an effective rather than a mathematically precise exponent, a restraining force to prevent divergence over long time is still required. Accordingly we introduce a negative dependence of the cell cycle time on an arbitrary combination of initial values of phenotype component. Previous work [17, 18, 19] has argued for such negative dependence from mathematical considerations supported by experimental correlation data. Here, our model provides the opportunity to investigate how the measured correlations might arise under different assumptions on cell-division control. The results of Fig. 5 were obtained from a model in which one phenotype component controls division, and as an outcome other components are correlated with cycle time as well. Thus negative correlation can arise in any measurable property without a direct feedback mechanism. One interpretation consistent with data is that cell size – the phenotype with the strongest measured correlations – is the primary component in determining cell division, whereas highly expressed proteins are to varying degrees indirectly correlated. However, equally consistent is the possibility that cell size itself exhibits indirect correlations with cycle-time whereas other, hidden, variables control division. From a more general perspective an important conclusion is that measured correlations involving global variables do not necessarily imply a direct mechanism by which one regulates the other.

An intriguing aspect of our data is the emergence of statistical properties that remain distinct between individual bacteria over dozens of generations, specifically, the long-time average of both cell size and content of different proteins. The commonly accepted approach to phenotypic variability assumes that a cell population is a statistical ensemble, with cells governed by the same dynamical system, and that individuals differ by their initial conditions and by different realizations of the stochastic processes (which are part of the dynamical system). Under these assumptions, one may expect the system to be ergodic: namely, that statistics over time can be replaced by statistics over the population. Such an assumption has been almost invariably made in previous studies of

phenotypic variability, but our data shows that for some quantities this property is violated. Such violation can result from at least two different scenarios. In one scenario, the governing dynamical system is still the same for all cells but due to the complex structure of phase space, trajectories starting from different initial conditions may be trapped and will not explore the entire space even for exceedingly long times. This effect has been studied theoretically in previous work [32], which assumed that dynamics is so slow for individual cells that protein content is essentially frozen in one of two states - very low or very high expression - during the time of observation. In contrast to this assumption, our experiments are performed in a regime where protein is highly produced and individual traces exhibit broad variability along time, i.e. they are far from being frozen. Still, these broad distributions cover different ranges, as shown in Fig. 3.

Alternatively, individual cells may in fact be governed by slightly different dynamical systems, or at least with different parameters. In this case there is no reason to expect that statistics of individual cells would be identical even for infinite time. The model presented here allows us to detect those parameters which are expected to influence the long-term averages and to estimate their values directly from the data. The results of this analysis show that the value of the feedback parameter regulating the cell-cycle time influences the long-term average, a prediction supported by the data. The multi-dimensional picture is indispensable in this analysis, since looking at each component separately enables to correlate only effective variables. In the case of protein content, it was found that its long-term average is correlated with feedback strength in another variable - cell length - providing a dynamical explanation for the non-ergodic nature of protein averages. Thus the feedback exerted by cell length on the cell-cycle manifests itself indirectly in properties of another phenotype component.

The dynamic model also predicts the effect of individual parameters on the shape of distributions of the different phenotype components. We have shown that this effect is extremely weak: first, all measured traces show a shape parameter which falls in a relatively narrow range. Since this shape parameter is a combination of dynamical parameters, this does not contradict the previous conclusion on the existence of distinct properties of individual cells. Second, the log-normal distribution predicted by the model exhibits a collapse after scaling to a good approximation within this measured range. This provides a possible explanation of the universal rescaling phenomenon observed in previous work, although the connection to the results on yeast cells remains to be investigated.

In addition to the average value of phenotype components, the correlation function is also distinct among individual traces. Some traces show damped oscillations, with distinct amplitude and frequency. This phenomenon, which has been reported recently [28], is a direct result of the discrete timescale dictated by cell division events. Our model, as well as other previous models which are equivalent to a discrete-time Langevin equation, predicts the appearance of such individual

oscillations. Recent theoretical work [31] provides an understanding of this phenomenon, which is purely of random origin.

The proposed model highlights the notion of both protein content and cell size as global cellular variables. Such global variables result from the integrated action of many processes and therefore are statistically correlated, to various degrees, with other variables. This notion is easily accepted for cell size, and is extended here to protein content. Most proteins in bacteria are highly expressed, with a relatively small effect of number fluctuations [10] and moreover their degradation is negligible over a cell-cycle [33, 34]. These properties result in their smooth accumulation within the cell cycle, which buffers many microscopic noise sources. Their global nature is also reflected in the correlation of their copy-number with cell-cycle time, and in the robustness of their distribution shape, as discussed above. The existence of multiple global variables suggests a non-traditional interpretation of observable quantities in cell biology. Rather than being connected to one another by causal relations, these variables are correlated with one another statistically even without such causal relations. There may be many weak and intermediate correlations rather than few strong connections. Moreover, since global variables may be affected by any number of other variables, from few to many, their sensitivity to perturbations may span an enormous range. In other words, some variables will be strong determinants of cellular behavior while others will have almost no effect on it. This is in line with the concept of sloppy systems describing many complex physical and biological systems [35, 36].

Our work leaves much to be answered. The identification of an effective parameter that links to the distinct features of individual traces immediately raises the question: what determines that parameter in individual cells? One possibility is that this feedback parameter is an emergent property of the cell which arises dynamically from complex interactions. Such dynamic feedback has been suggested as an organizing principle for mesoscopic-scale systems [37]. This question is beyond the scope of our current work. Our ability to answer it is limited by the number of long traces presently available and the time of observation. Moreover this kind of data are in principle limited by the cell lifetime. How the initial conditions come into play is also unknown since these are determined by previous generations. New experimental systems may be designed to address this challenge.

Finally, the link of individual cells to the population, namely the level of the lineage, is another gap that remains to be bridged. How statistical properties in a population develop from single cells depend not only on the long-term behavior of specific cells, but also on the distribution of properties in a lineage [15]. This problem also awaits further experimental and theoretical studies.

Methods

Experimental procedure and data processing. Wild type MG1655 *E. coli* bacteria were used in all experiments described. Protein content was measured through the fluorescence intensity of green fluorescent protein (GFP) or red fluorescent protein (tdTomato) inserted into the bacteria on a high or medium copy number plasmid and expressed under the control of the promoter of interest. For measuring the expression level of a metabolically relevant protein, GFP was expressed from the medium copy number plasmid pZA [38] under the control of the Lac Operon (LacO) promoter. For metabolically irrelevant protein, GFP was expressed from the same plasmid pZA but under the control of the viral λ -phage promoter. For simultaneous measurement of the expression of two proteins, GFP was expressed from the high copy number plasmid pUC19 under the control of the LacO promoter, while tdTomato was expressed from the pZA plasmid under the control of the λ -phage promoter. The cultures were grown over night at 30°C, in M9 minimal medium supplemented with 1g/l casamino acids and 4g/l lactose (M9CL, for measuring the expression level from the LacO Promoter or both promoters together), or 4g/l glucose (M9CG, for measuring the expression level from the λ -promoter only). The following day, the cells were diluted in the same medium and regrown to early exponential phase, Optical Density (OD) between 0.1 and 0.2. When the cells reached the desired OD, they were concentrated 10X into fresh medium, and loaded into a microfluidic trapping device [13, 11]. After cells were trapped in the device, fresh medium was flown continuously through it to supply nutrients. The cells were allowed to grow in this device for 10s of generations, while maintaining the temperature fixed, using a made-in-house incubator. For more details of the experimental setup (see [13]). Images of the channels were acquired every 3 to 6 minutes in phase contrast and fluorescence modes using a Zeiss Axio Observer microscope with a 100x objective. The size and protein content of the mother cell were measured from these images using the image analysis software microbeTracker [39]. These data were then used to generate traces such as those presented in Fig. 1, and for further analysis as detailed in the main text.

Experimental data analysis Single-cell traces were analyzed using home-made MATLAB programs. Sample autocorrelation functions, Pearson correlation coefficients, sample distributions and linear curve fitting were all calculated by their implementations in MATLAB toolboxes. All sample autocorrelation function calculations followed a 3-point-average smoothing of the measured base-point values. Effective feedback parameters β_L and β_P were estimated for each trace separately, as the slope of the linear fit to scatter plots of generation duration (scaled by dividing by its trace-mean) as a function of logarithmic basepoints of cell-length or protein fluorescence, respectively (plots similar to Fig. 2).

Model implementation The model was implemented in a MATLAB program. Simulations were carried out for model systems of various dimensions N ; since most results were qualitatively sim-

ilar for a wide range of N , all simulation shown are for $N = 5$. Sample traces comprised 90 generations, where in each generation the linear dynamics were integrated over the interval $[0, T_n)$, with a time-step of $dt = 0.1$. In each simulation run, corresponding to a single-cell trace, the effective interaction matrix K was initialized with independent and identically distributed random elements, drawn from a uniform distribution on the interval $[0, 0.2]$. At each division event, to each element K_{ij} of K was added a different zero-mean Gaussian random variable with standard deviation $\sigma = 0.1 \cdot \sqrt{K_{ij}}$. At each division event, a division ratio was drawn independently (among generations and among components within the generation) from a Gaussian distribution centered at 0.5 and with standard deviation $\sigma = 0.1$. A zero-mean Gaussian random variable ξ , with standard deviation $\sigma = 0.25$ was added to the cycle time in each generation. The remaining parameters were taken to be $T = \ln 2$ and $\beta \in [0.5, 1.5]$ for one component only and the rest zero.

Acknowledgements This work was supported by the US-Israel Binational Science Foundation (NB and HS). This research was supported by The Israel Science Foundation (grant No. 1566/11; NB). HS acknowledges the support of NSF Grant PHY-1401576. We thank Omri Barak, Erez Braun, Yoni Savir and Dan Stein for helpful comments.

References

- [1] Arjun Raj and Alexander van Oudenaarden. Nature, nurture, or chance: stochastic gene expression and its consequences. *Cell*, 135(2):216–226, 2008.
- [2] Johan Paulsson. Models of stochastic gene expression. *Physics of life reviews*, 2(2):157–175, 2005.
- [3] Alvaro Sanchez and Ido Golding. Genetic determinants and cellular constraints in noisy gene expression. *Science*, 342(6163):1188–1193, 2013.
- [4] Vahid Shahrezaei and Samuel Marguerat. Connecting growth with gene expression: of noise and numbers. *Current opinion in microbiology*, 25:127–135, 2015.
- [5] Noreen Walker, Philippe Nghe, and Sander J Tans. Generation and filtering of gene expression noise by the bacterial cell cycle. *BMC biology*, 14(1):1, 2016.
- [6] Daniel J Kiviet, Philippe Nghe, Noreen Walker, Sarah Boulineau, Vanda Sunderlikova, and Sander J Tans. Stochasticity of metabolism and growth at the single-cell level. *Nature*, 514(7522):376–379, 2014.
- [7] H. Salman, N. Brenner, C.-K. Tung, N. Elyahu, E. Stolorovicki, L. Moore, A. Libchaber, and E. Braun. Universal protein fluctuations in populations of microorganisms. *Phys. Rev. Lett*, 108:238105, 2012.

- [8] Lindsay S Moore, Elad Stolovicki, and Erez Braun. Population dynamics of metastable growth-rate phenotypes. *PloS one*, 8(12):e81671, 2013.
- [9] C. Furasawa, T. Suzuki, A. Kashiwagi, T. Yomo, and K. Kaneko. Ubiquity of log-normal distributions in intra-cellular reaction dynamics. *Biophysics*, 1:25–31, 2005.
- [10] Y. Taniguchi, P.J. Choi, G.-W. Li, H. Chen, M. Babu, J. Hearn, A. Emili, and X.S. Xie. Quantifying e. coli proteome and transcriptome with single-molecule sensitivity in single cells. *Science*, 329:533, 2010.
- [11] Ping Wang, Lydia Robert, James Pelletier, Wei Lien Dang, Francois Taddei, Andrew Wright, and Suckjoon Jun. Robust growth of escherichia coli. *Current biology*, 20(12):1099–1103, 2010.
- [12] Srividya Iyer-Biswas, Charles S Wright, Jonathan T Henry, Klevin Lo, Stanislav Burov, Yihan Lin, Gavin E Crooks, Sean Crosson, Aaron R Dinner, and Norbert F Scherer. Scaling laws governing stochastic growth and division of single bacterial cells. *Proceedings of the National Academy of Sciences*, 111(45):15912–15917, 2014.
- [13] N. Brenner, E. Braun, A. Yoney, L. Susman, J. Rotella, and H. Salman. Single-cell protein dynamics reproduce universal fluctuations in cell populations. *Eur. Phys. J E*, 38:102, 2015.
- [14] Andrew S Kennard, Matteo Osella, Avelino Javier, Jacopo Grilli, Philippe Nghe, Sander J Tans, Pietro Cicuta, and Marco Cosentino Lagomarsino. Individuality and universality in the growth-division laws of single e. coli cells. *Physical Review E*, 93(1):012408, 2016.
- [15] Denis Cottinet, Florence Condamine, Nicolas Bremond, Andrew D Griffiths, Paul B Rainey, J Arjan GM de Visser, Jean Baudry, and Jérôme Bibette. Lineage tracking for probing heritable phenotypes at single-cell resolution. *PloS one*, 11(4):e0152395, 2016.
- [16] Mats Wallden, David Fange, Ebba Gregorsson Lundius, Özden Baltekin, and Johan Elf. The synchronization of replication and division cycles in individual e. coli cells. *Cell*, 166(3):729–739, 2016.
- [17] A. Amir. Size regulation in bacteria. *Phys. Rev. Lett.*, 112:208102, 2014.
- [18] N. Brenner, C. M. Newman, D. Osmanovic, Y. Rabin, H. Salman, and D. L. Stein. Universal protein distributions in a model of cell growth and division. *Phys. Rev. E*, 92:042713, 2015.
- [19] A. S. Kennard J. Grilli, M. Osella and M. C. Lagomarsino. Relevant parameters in models of cell division control. *arxiv 1606.09284*, 2016.
- [20] Fabai Wu and Cees Dekker. Nanofabricated structures and microfluidic devices for bacteria: from techniques to biology. *Chemical Society Reviews*, 45(2):268–280, 2016.

- [21] M. Osella, E. Nugentc, and M. C. Lagomarsino. Concerted control of escherichia coli cell division. *PNAS*, 111(9):34313435, 2014.
- [22] L. Robert, and A. Amir. Single-cell analysis of growth in budding yeast and bacteria reveals a common size regulation strategy. *Cell - Current Biology*, 26:356–361, 2016.
- [23] S. Taheri-Araghi, S. Bradde, J. T. Sauls, N. S. Hill, P. A. Levin, J. Paulsson, M. Vergassola, and S. Jun. Cell-size control and homeostasis in bacteria. *Curr. Biol.*, 25(3):385–391, 2015.
- [24] A. Adiciptaningrum, M. Osella, M. C. Moolman, M. C. Lagomarsino, and S. J. Tans. Stochasticity and homeostasis in the e. coli replication and division cycle. *Nature - Scientific Reports*, 5(18261), 2015.
- [25] Michel Godin, Francisco Feijó Delgado, Sungmin Son, William H Grover, Andrea K Bryan, Amit Tzur, Paul Jorgensen, Kris Payer, Alan D Grossman, Marc W Kirschner, et al. Using buoyant mass to measure the growth of single cells. *Nature methods*, 7(5):387–390, 2010.
- [26] Manuel Campos, Ivan V Surovtsev, Setsu Kato, Ahmad Paintdakhi, Bruno Beltran, Sarah E Ebmeier, and Christine Jacobs-Wagner. A constant size extension drives bacterial cell size homeostasis. *Cell*, 159(6):1433–1446, 2014.
- [27] L. Robert, M. Hoffmann, N. Krell, S. Aymerich, J. Robert, and M. Doumic. Division in escherichia coli is triggered by a size-sensing rather than a timing mechanism. *BMC Biology*, 2014.
- [28] Y. Tanouchi, A. Pai, H. Park, S. Huang, R. Stamatov, N. E. Buchler, and L. You. A noisy linear map underlies oscillations in cell size and gene expression in bacteria. *Nature*, 523:357360, 2015.
- [29] Cyril N Hinshelwood. On the chemical kinetics of autotrophic systems. *Journal of the Chemical Society (Resumed)*, pages 745–755, 1952.
- [30] S. Iyer-Biswas, G. E. Crooks, and N. F. Scherer and A. R. Dinner. Universality in stochastic exponential growth. *Phys. Rev. Lett*, 113:028101, 2014.
- [31] W. I. Newman. Emergence of patterns in random processes. ii. stochastic structure in random events. *Phys. Rev. E*, 89(062113), 2014.
- [32] Andrea Rocco, Andrzej M Kierzek, and Johnjoe McFadden. Slow protein fluctuations explain the emergence of growth phenotypes and persistence in clonal bacterial populations. *PloS one*, 8(1):e54272, 2013.

- [33] KL Larrabee, JO Phillips, GJ Williams, and AR Larrabee. The relative rates of protein synthesis and degradation in a growing culture of *escherichia coli*. *Journal of Biological Chemistry*, 255(9):4125–4130, 1980.
- [34] Christian Trötschel, Stefan P Albaum, and Ansgar Poetsch. Proteome turnover in bacteria: current status for *corynebacterium glutamicum* and related bacteria. *Microbial biotechnology*, 6(6):708–719, 2013.
- [35] J. Sethna. Fitting exponentials: prediction without parameters. <http://www.lasp.cornell.edu/sethna/Sloppy/FittingExponentials.html>.
- [36] Mark K Transtrum, Benjamin B Machta, Kevin S Brown, Bryan C Daniels, Christopher R Myers, and James P Sethna. Perspective: Sloppiness and emergent theories in physics, biology, and beyond. *The Journal of chemical physics*, 143(1):010901, 2015.
- [37] Robert B Laughlin, David Pines, Joerg Schmalian, Branko P Stojković, and Peter Wolynes. The middle way. *Proceedings of the National Academy of Sciences*, 97(1):32–37, 2000.
- [38] Rolf Lutz and Hermann Bujard. Independent and tight regulation of transcriptional units in *escherichia coli* via the *lac*r/o, the *tet*r/o and *ara*c/i1-i2 regulatory elements. *Nucleic acids research*, 25(6):1203–1210, 1997.
- [39] Oleksii Sliusarenko, Jennifer Heinritz, Thierry Emonet, and Christine Jacobs-Wagner. High-throughput, subpixel precision analysis of bacterial morphogenesis and intracellular spatio-temporal dynamics. *Molecular microbiology*, 80(3):612–627, 2011.

Supplementary Information

SI1: Distinct long-term statistics of individual cells

In this Appendix we present results on distinct individual long-term statistics, as evident from single-cell traces measured independently in another lab. We analyzed cell-length and protein content measurements from publicly available data [11]. Fig. 9 presents an accumulating average along traces of both cell-length (A) and protein content (B). Here too as in our data the accumulating average of each trace shows fluctuations over small time windows and convergence to a distinct average over the entire length of the experiment. The temporal averages of both properties measured span a smaller range in this dataset in comparison to ours. Protein content has a range of $\approx 30\%$ and cell-length a range of $\approx 12\%$. It is noted that cells were grown in a different medium and thus some differences are expected.

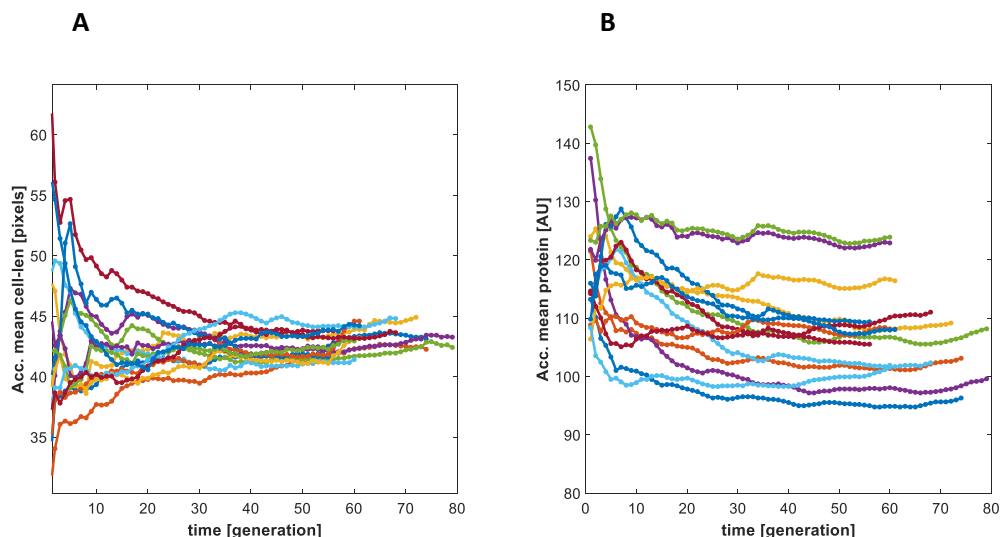


Figure 9: Individuality building up along time in an independent study. Accumulating mean cell-length (A) and protein fluorescence (B) along the traces, each trace with a different color, as a function of time window of averaging. The plots show statistics for traces that have stationary distributions and have between 40 and 100 generations, all taken from the sub-directory "E. coli MG1655 *lexA3*/20090930" of the data-set published in [11]), altogether 16 traces were analyzed.

Distinct long-term autocorrelations along individual traces are also observed on this data-set. Fig. 10 shows the correlation functions of 10 different traces (each at least 50 generations long), where it is seen that each one has distinct slow modulations. The averaged correlation function of all traces exhibits, as in our data, a smoother decay.

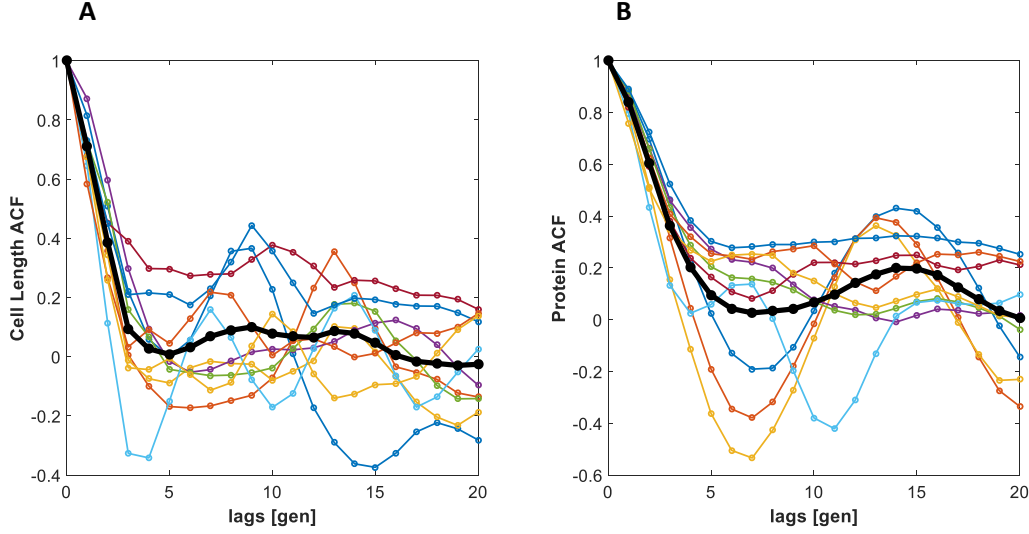


Figure 10: Long-term correlations in an independent study. Sample-path correlation functions from 10 individual traces from the corpus described in Fig. 9. Panel (A) shows correlation functions of cell-length basepoints, panel (B) of protein content basepoints. Bold black line is the average over all correlation functions.

SI2: Properties of the effective interaction model

As mentioned in the main text, all qualitative properties presented in the main text are reproduced by our model, regardless of the dimensionality of K or of the exact values of its components. Specifically, simulations of our model with $N = 2$ to $N = 100$ were conducted, where each simulation had as initial conditions a matrix with randomly and independently chosen components. All phenomenology presented in Figures 1 to 4 in the main text were reproduced for each value of N .

Variability across generations of the effective exponential accumulation rates does not depend on the small changes across generations in the effective interaction matrix K . Here we demonstrate this point by simulating a fixed K model, namely $K_n \equiv K$ for all generations n in the trace; the matrix is arbitrary and chosen at random at the beginning of the simulation. Fig. 11 shows the resulting per-cycle accumulation from such a simulated trace, and their fit to exponential functions. A wide variability of the effective exponential rate is seen among cycles, which results from reshuffling of the initial conditions at the beginning of each cell-cycle by random partitioning at division.

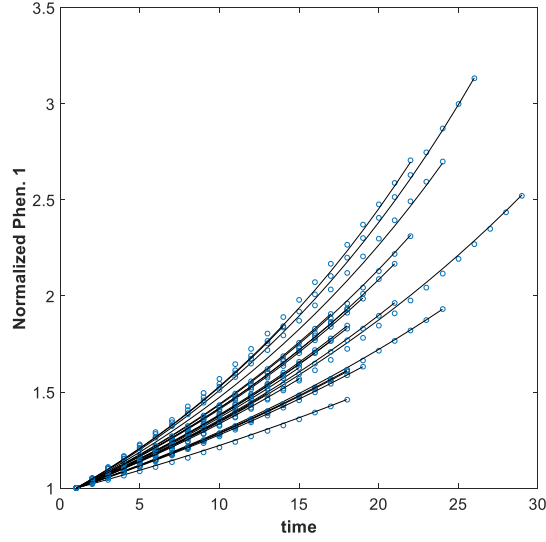


Figure 11: Variable effective exponential accumulation in fixed K model. Traces normalized to initial time and to value 1 at the cell-cycle start, emphasizing the variability between generations of the effective exponents. Black lines represent the fitted exponential accumulation curve.

The small random changes introduced in K at division affect only the correlations between effective exponents across generations. For a fixed K model, the effective exponents corresponding to different components are generally negatively correlated, as a result of a compensation that occurs from the exactly conserved eigenvalues. Note also, that the random changes introduced in K at division do not lead to the divergence of K . This is due to the relatively small changes and the finite lifetime of the cell.

SI3: Effective feedback

In the main text results were presented for a special case of the model, namely $\beta_1 > 0$ and $\beta_i = 0$ for $i > 1$. This represents a system where one phenotype component controls the timing of cell division. In this case, our numerical results indicated that an effective restraining force acts on all components, and emerges as correlation between cycle-time and the basepoint values of the various components. Here we derive this effective restraining force by direct calculation in our model. For simplicity, we choose to treat the two-dimensional case; higher dimensional cases are in principle the same.

Assume two phenotype components $x^{(1)}$ and $x^{(2)}$, evolving within the n th cycle as

$$\frac{d}{dt} \begin{pmatrix} x_n^{(1)} \\ x_n^{(2)} \end{pmatrix} (t) = K \begin{pmatrix} x_n^{(1)} \\ x_n^{(2)} \end{pmatrix} (t),$$

and the inter-division time is chosen as

$$T_n = \bar{T} - \beta \ln x_n^{(1)}(0) + \xi_n.$$

At the end of each cycle, the phenotype components are

$$x_n^{(1)}(T_n) = c_1 e^{\lambda_1 T_n} v_{11} + c_2 e^{\lambda_2 T_n} v_{12} \quad (8)$$

$$x_n^{(2)}(T_n) = c_1 e^{\lambda_1 T_n} v_{21} + c_2 e^{\lambda_2 T_n} v_{22} \quad (9)$$

where λ_i are the eigenvalues of K , V is the matrix representation for the eigenbasis of K , and

$$c = \begin{pmatrix} c_1 \\ c_2 \end{pmatrix} = V^{-1} \begin{pmatrix} x_n^{(1)}(0) \\ x_n^{(2)}(0) \end{pmatrix}.$$

By equations 8 and 9 we see that at the end of each cycle, the two phenotype components are both (differently) weighted sums of the same two random variables $c_j e^{\lambda_j T_n}$, $j = 1, 2$. Note that these variables are functions of the phenotype initial conditions at cycle n , $x_n^{(1)}(0)$ and $x_n^{(2)}(0)$. We can then express $x_n^{(1)}(T_n)$ as a function of $x_n^{(2)}(T_n)$ such:

$$\begin{aligned} x_n^{(1)}(T_n) &= \frac{v_{11}}{v_{21}} x_n^{(2)}(T_n) + c_2 e^{\lambda_2 T_n} \left(v_{12} - \frac{v_{22}}{v_{21}} \right) \\ &= a x_n^{(2)}(T_n) + b_n, \end{aligned} \quad (10)$$

where a is constant and b_n is a random variable. In our model, consecutive cycles are linked via the relation

$$x_{n+1}^{(1)}(0) = f_n^{(1)} x_n^{(1)}(T_n), \quad (11)$$

$$x_{n+1}^{(2)}(0) = f_n^{(2)} x_n^{(2)}(T_n), \quad (12)$$

where $f_n^{(1)}$ and $f_n^{(2)}$ are the division ratios of the two respective components. In logarithmic coordinates the above two equations are given by

$$\ln x_{n+1}^{(1)}(0) = \ln f_n^{(1)} + \ln x_n^{(1)}(T_n),$$

$$\ln x_{n+1}^{(2)}(0) = \ln f_n^{(2)} + \ln x_n^{(2)}(T_n).$$

Substituting Eq. 10 into the above yields

$$\ln x_{n+1}^{(1)}(0) = \ln f_n^{(1)} + \ln \left[a x_n^{(2)}(T_n) + b_n \right]$$

$$= \ln \left[\frac{f_n^{(1)} a}{f_n^{(2)}} x_{n+1}^{(2)}(0) + b_n \right].$$

This result shows how basepoints of different phenotype components are correlated across cell cycles.

Now, based on the effective exponential approximation α_n , we have the relation

$$x_{n+1}^{(1)}(0) = f_n^{(1)} x_n^{(1)}(0) e^{\alpha_n^{(1)} T_n}, \quad (13)$$

$$x_{n+1}^{(2)}(0) = f_n^{(2)} x_n^{(2)}(0) e^{\alpha_n^{(2)} T_n}, \quad (14)$$

by which we can approximate $\ln x_{n+1}^{(2)}(0)$ as a discrete Langevin mapping:

$$\begin{aligned} \ln x_{n+1}^{(2)}(0) &= \ln f_n^{(2)} + \ln x_n^{(2)}(0) + \alpha_n^{(2)} T_n \\ &= \ln f_n^{(2)} + \ln x_n^{(2)}(0) + \alpha_n^{(2)} \left((\bar{T} + \xi_n) - \beta \ln x_n^{(1)}(0) \right) \\ &= \ln f_n^{(2)} + \ln x_n^{(2)}(0) + \alpha_n^{(2)} \left((\bar{T} + \xi_n) - \beta \ln \left[\frac{f_{n-1}^{(1)} a}{f_{n-1}^{(2)}} x_n^{(2)}(0) + b_{n-1} \right] \right) \end{aligned} \quad (15)$$

$$= \ln f_n^{(2)} + \underbrace{\left(1 - \alpha_n^{(2)} \beta \right) \ln x_n^{(2)}(0)}_{\text{indirect feedback}} + \alpha_n^{(2)} (\bar{T} + \xi_n) - \delta_n. \quad (16)$$

The term

$$\delta_n = \alpha_n^{(2)} \beta \ln \left(1 + \frac{b_{n-1} f_{n-1}^{(2)}}{x_n^{(2)}(0) f_{n-1}^{(1)} a} \right)$$

includes the residual terms from the logarithm in Eq. 15, which depends on the second phenotype component $x_n^{(2)}(0)$. Thus, we expect the strength of measured effective restraining force $\tilde{\beta}$ to differ from β , and we write the effective mapping process as

$$\ln x_{n+1}^{(2)}(0) = \ln f_n^{(2)} + \left(1 - \alpha_n^{(2)} \tilde{\beta} \right) \ln x_n^{(2)}(0) + \alpha_n^{(2)} (\bar{T} + \xi_n).$$

SI4: Mean-field approximation

Our proposed model consists of relatively simple building blocks. Nevertheless, when put together, a complex relation between consecutive basepoint values of each component arises from the discrete process

$$x_{n+1}^{(j)} = f_n^{(j)} \cdot x_n^{(j)}(T_n), \quad (17)$$

as defined in the main text. We derive an approximation for this mapping, and utilize it to calculate the steady-state distribution of per-coordinate basepoint values.

Approximating the trajectory within each cell-cycle by an effective exponential rate, the evolution of each component $1 \leq j \leq N$ of the phenotype basepoint vector \vec{x}_n follows the simplified mapping

$$x_{n+1}^{(j)} = f_n^{(j)} x_n^{(j)} e^{\alpha_n^{(j)} T_n}. \quad (18)$$

Taking the natural logarithm of (18) we have

$$\begin{aligned} \ln x_{n+1}^{(j)} &= \ln f_n^{(j)} + \ln x_n^{(j)} + \alpha_n^{(j)} T_n \\ &= \ln f_n^{(j)} + \ln x_n^{(j)} + \alpha_n^{(j)} \left(\bar{T} - \sum_{i=1}^N \beta_i \ln x_n^{(i)} + \xi_n \right) \\ &= \ln f_n^{(j)} + \left(1 - \alpha_n^{(j)} \beta_j \right) \ln x_n^{(j)} + \alpha_n^{(j)} \left(\bar{T} - \sum_{i \neq j} \beta_i \ln x_n^{(i)} + \xi_n \right). \end{aligned} \quad (19)$$

Collecting all contributions from components other than j into the mean-field variable

$$E_n^{(j)} := \sum_{i \neq j} \beta_i \ln x_n^{(i)},$$

dropping the superscript j for convenience, and denoting the logarithmic coordinate by $y_n := \ln x_n$ we write Eq. 19 as

$$y_{n+1} = \ln f_n + (1 - \alpha_n \beta) y_n + \alpha_n \bar{T} + \alpha_n \xi_n - \alpha_n E_n.$$

We further simplify our analysis by using the average effective exponential rate along the entire trace, i.e.

$$\alpha_n \equiv \alpha.$$

In addition, defining the additive term

$$\eta_n = \ln f_n + \alpha \bar{T} + \alpha \xi_n - \alpha E_n$$

yields a discrete-time Langevin equation

$$y_{n+1} = (1 - \alpha \beta) y_n + \eta_n. \quad (20)$$

To account for the effective feedback, arising from correlations with other phenotype components which directly contribute to feedback, we define $\tilde{\beta}$ and $\tilde{\eta}_n$. These are the result of moving all indirect feedback terms from η_n to be included in $\tilde{\beta}$ (as derived in SI3); the result is the mapping process

$$y_{n+1} = (1 - \alpha \tilde{\beta}) y_n + \tilde{\eta}_n,$$

which is comparable to experimental measurements.

Finally, assuming $\hat{\eta}_n$ is Normally distributed and independent along generations, the stationary limiting distribution of Eq. 20 can be shown to be Normal, as described in [18].

SI5: Long-term correlations in effective exponents

Fig. 12 shows the long-term correlation in the dynamics of the effective exponential accumulation rates. The accumulation rates are obtained from fitting both cell-length and protein content traces, in each cell-cycle, to a single exponential function.

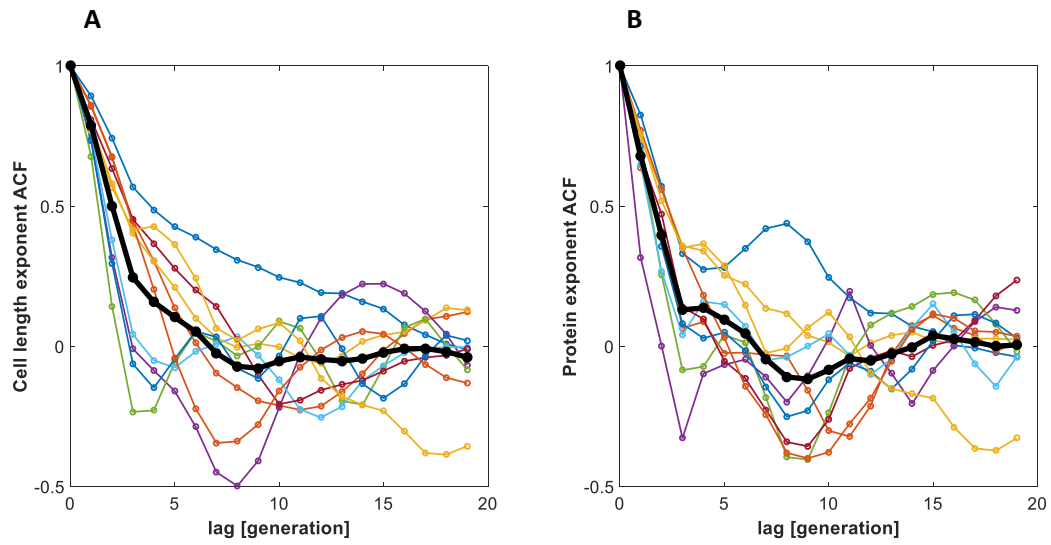


Figure 12: Accumulation exponent correlation functions. Colored lines show the autocorrelation of the effective exponential accumulation rates for each trace, both for cell-length (A) and for LAC regulated protein (B). Each trace exhibits a different pattern of correlation which persists over many generations. These patterns are washed out by averaging between traces. Bold black curves shows the average of all correlation functions;

SI6: Distinct individual statistical properties in model traces

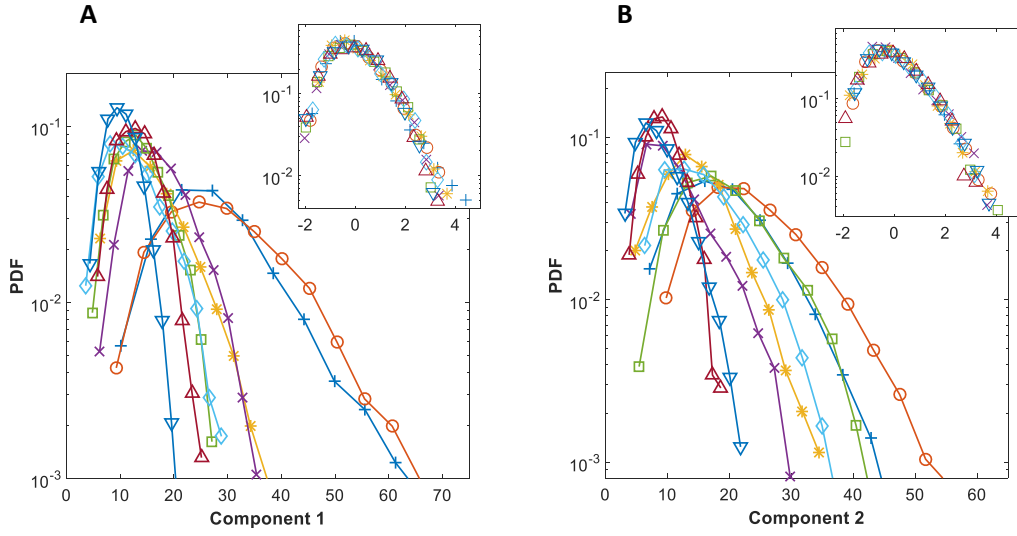


Figure 13: Model sample-path distributions. Distributions of first (A) and second (B) phenotype components in calculated along 8 different traces (color code). Each trace was generated by simulating our model with varying values of feedback β (which was associated only with the first component, see main text), while all other parameters were fixed. Insets: the same distributions in scaled variables. Both phenotype component exhibit a collapse of scaled distributions onto a single universal curve.

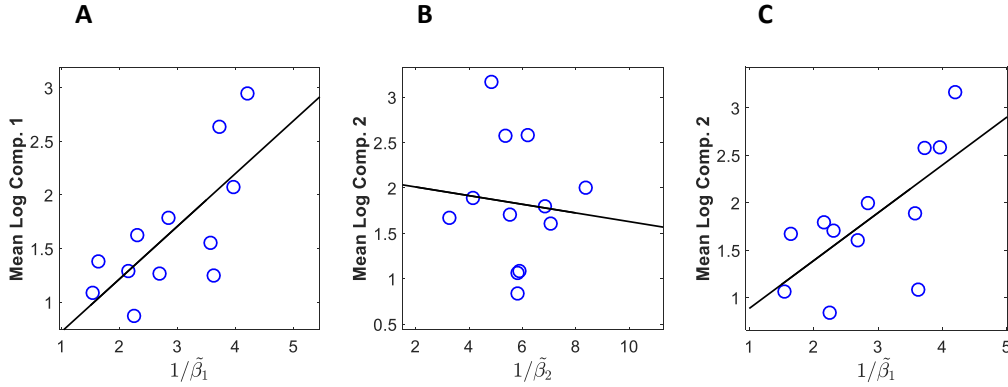


Figure 14: Model reproduction of the non-universal trace average. (A) Dependence of average (log) first component on the measured inverse strength of restraining force on the first component, $1/\tilde{\beta}_1$. A linear relation is observed (correlation coefficient $CC \approx 0.72$). (B) Dependence of average (log) second component on measured inverse strength of second component restraining force $\tilde{\beta}_2$. No significant dependence is seen (correlation coefficient $CC \approx -0.09$). (C) Dependence of average (log) second component on inverse strength of first component restraining force $1/\tilde{\beta}_1$ (correlation coefficient $CC \approx 0.68$). In all panels black line represents the best linear fit to the data points.

SI7: Shapes of the lognormal distribution

As shown in the main text, the parameters extracted from the experimental protein and cell-length traces, when applied to the mean-field approximation of the model, predict a lognormal distribution with shape parameter in the range 0.3-0.5. While mathematically each value defines a different shape, for a finite sampling this range of values gives rise to similar shapes that may be difficult to distinguish experimentally. This appendix demonstrates the different shapes that can arise with a broader range of shape parameters for the lognormal distribution, when rescaled linearly as in the experimental studies. It shows that in general the lognormal distribution can span a range of significantly different shapes.

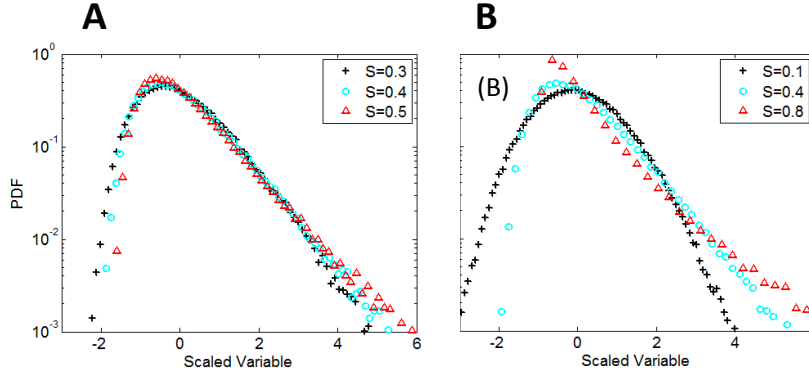


Figure 15: Different shapes of the scaled Lognormal distribution. (A) The range of shape parameters S measured in our experiments span a range of shapes that are similar under linear scaling, namely, subtraction of mean and division by standard deviation. (B) A broader range of shape parameters defines a family of lognormal distributions that do not collapse under linear scaling.

SI8: Accuracy of mean peak-to-peak distance

In the main text we have shown that our experimental results generally follow the prediction developed in [31], with a rather large spread around the theoretical curve. Here we show numerically

that the consistency of the mean peak-to-peak measure scales with the length of the time-series in question. For this purpose, we simulate many realizations of discrete Langevin equations

$$x_{n+1} = (1 - \nu) x_n + \eta_n \quad (21)$$

while varying the dynamic parameter ν between realizations. We repeat this procedure for processes of three different lengths: short (50 time-steps, which is the number of generations in a typical measured trace), intermediate (200 time-steps) and long (1000 time-steps). Fig. 16A illustrates the results of this simulation, where it is seen that the "short" corpus is scattered around the theoretical curve similar to our experimental data. This analysis highlights the sensitivity of this measure to the length of the mapping process. It is expected that, once obtained experimentally, traces of intermediate or long lengths should show a higher consistency with the theory.

In addition, in Fig. 16B we further emphasize the persistence of temporal correlation in long traces. This figure shows correlation functions calculated along four model realizations, each with a different dependence parameter. Each trace exhibits distinct correlations spanning many generations; the existence of these oscillations in the correlation functions of such long traces rule out the idea that long-term temporal correlations originate from finite-size effects of short traces.

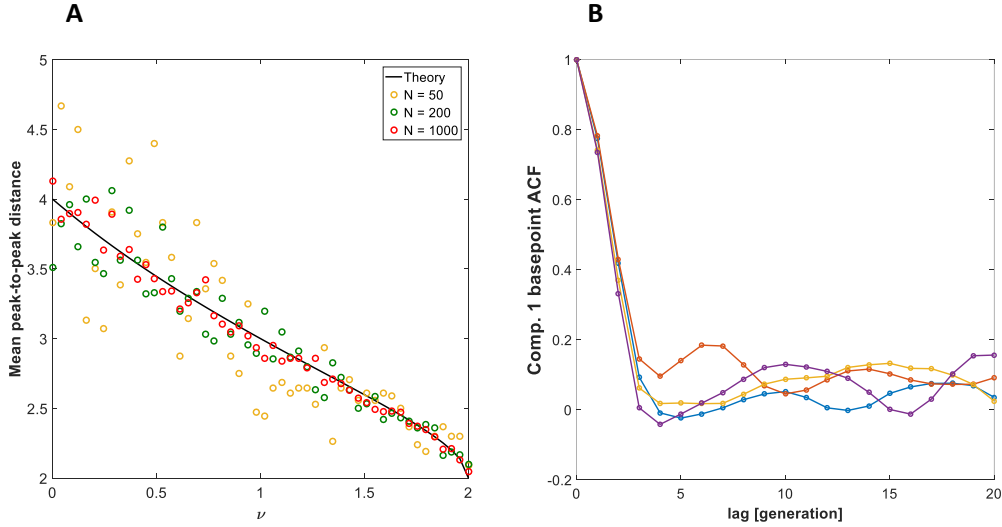


Figure 16: Accuracy of the mean peak-to-peak distance. (A) Mean peak-to-peak distance as a function of the regulation parameter ν , calculated on realizations of the discrete Langevin mapping $x_{n+1} = (1 - \nu) x_n + \eta_n$. Different colors correspond to realizations of different lengths; black line is the theoretical prediction. We quantify consistency with the prediction by computing the mean square error between the theoretical curve and each corpus of realization lengths; the error is 0.12, 0.025 and 0.006 for lengths $N = 50$, $N = 200$ and $N = 1000$ respectively. (B) Correlation functions calculated along four different model realizations, with varying dependence parameter. Each trace contains 1000 generations.